Volume 7
Number 22
21 November 2025
Pages 7051–7410

Nanoscale Advances

rsc.li/nanoscale-advances

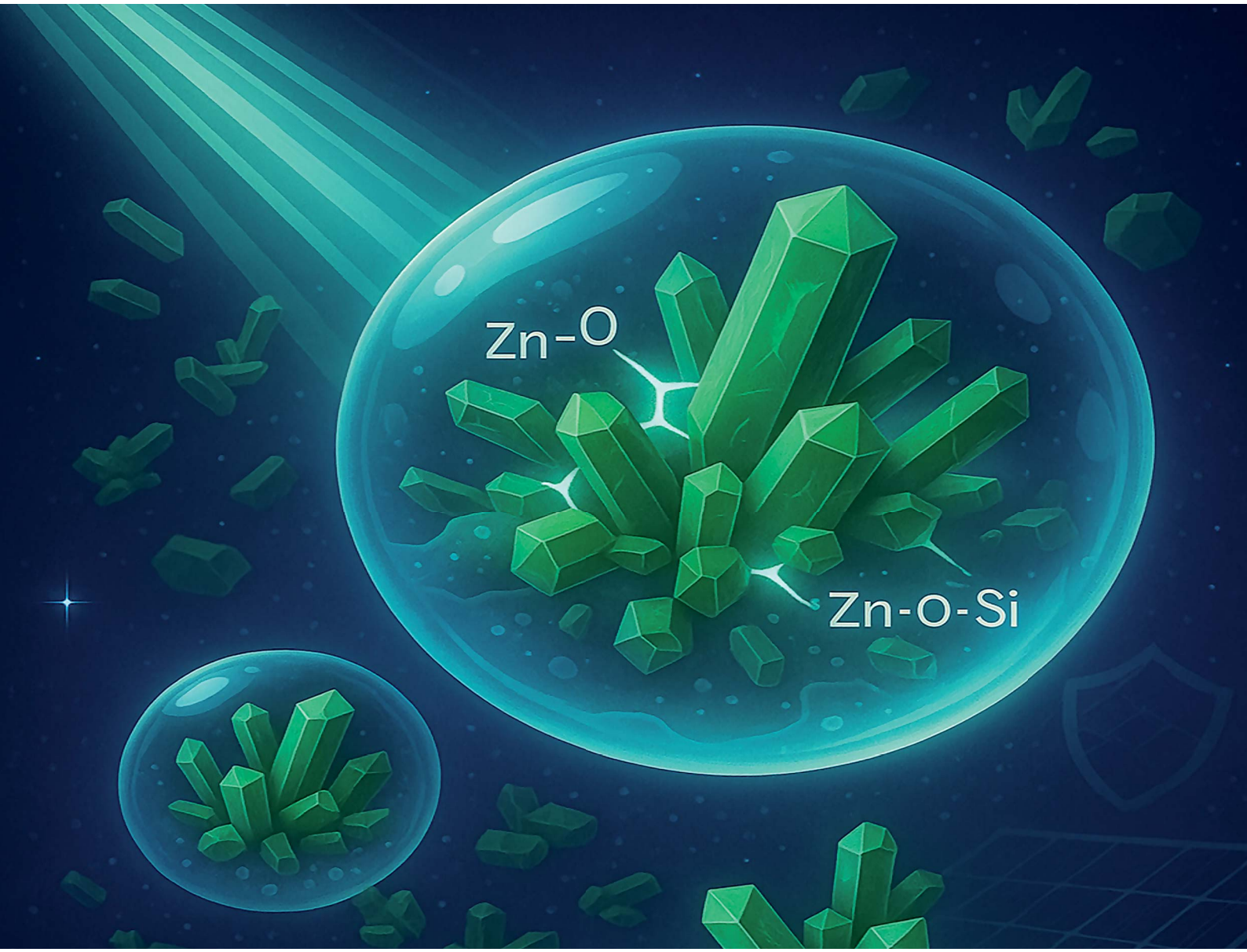

ISSN 2516-0230

ROYAL SOCIETY OF CHEMISTRY

PAPER

S. Abedrabbo *et al.*

Sol–gel synthesis and characterization of ZnO–SiO_2 nanocomposites: a comparative study with pure ZnO and SiO_2

NCNST

Nanoscale Advances

ROYAL SOCIETY OF CHEMISTRY

PAPER

View Article Online
View Journal | View Issue

Cite this: *Nanoscale Adv.*, 2025, **7**, 7145

Sol–gel synthesis and characterization of ZnO–SiO_2 nanocomposites: a comparative study with pure ZnO and SiO_2

A. Samuel,[a] A. Abdullah,[b] G. Xavier,[c] S. Stephen,[c] M. M. Zeidan,[d] D. Choi[b] and S. Abedrabbo *[e]

In this investigation, pure SiO_2, ZnO, and ZnO–SiO_2 (10 : 90) nanocomposites were synthesized *via* the sol–gel method and systematically characterized in a comparative framework. Upon increasing the annealing temperature, the ZnO–SiO_2 composite predominantly retained its amorphous character, with the emergence of distinct ZnO diffraction peaks. Structural analysis using X-ray diffraction (XRD) confirmed the presence of the wurtzite phase in ZnO, alongside the intrinsically amorphous nature of the SiO_2 matrix. Fourier-transform infrared (FT-IR) spectroscopy provided clear evidence for the formation of Zn–O–Si bonds, in addition to the characteristic Si–O–Si and Zn–O vibrational modes. Scanning electron microscopy coupled with energy-dispersive X-ray spectroscopy (SEM–EDS) revealed a homogeneous elemental distribution within the synthesized nanocomposite. This work underscores the pronounced influence of thermal treatment on interfacial structure and crystallinity, offering insights into the tailored design of ZnO–SiO_2 nanocomposites through controlled annealing.

Received 22nd June 2025
Accepted 1st October 2025

DOI: 10.1039/d5na00612k

rsc.li/nanoscale-advances

1. Introduction

The synthesis of SiO_2 and ZnO nanocomposites has attracted considerable interest, owing to their wide-ranging applications in catalysis, optoelectronics, and environmental remediation. SiO_2 is a well-established electrical insulator and serves as the material of choice for gate oxides in the majority of complementary-metal-oxide-semiconductor (CMOS) transistors. Its intrinsically high surface area and thermal stability renders its extensive utilization as a catalyst support, facilitating enhanced catalytic processes such as pollutant degradation, water dissociation, and selective oxidation—especially when paired with active materials like TiO_2 or CdS.[1,2] The chemically inert nature of SiO_2 makes it an exceptional matrix for stabilizing metal oxides, effectively inhibiting particle agglomeration and enhancing performance under extreme conditions.[3] Notably, Roßkopf *et al.* demonstrated that doping SiO_2 nanoparticles could efficiently suppress reactant agglomeration during repeated thermal cycling, as evidenced by heat storage and release experiments conducted over ten cycles.[4]

In contrast, ZnO is a multifunctional semiconductor distinguished by its direct wide bandgap of approximately 3.37 eV, which is highly advantageous for ultraviolet (UV)-based optoelectronic devices, photodetectors, and transparent conducting films—supporting its adoption as a coating material for photovoltaic modules. The unique properties of ZnO have generated substantial interest in recent years.[5] ZnO is widely deployed in gas sensors for the detection of analytes such as NO_2, H_2S, ethanol, and ammonia, which is critical for environmental monitoring and industrial safety applications.[6] Additionally, ZnO displays potent antimicrobial activity, enabling its integration into biomedical coatings, self-cleaning surfaces, and food packaging materials.[7] Its remarkable photocatalytic capabilities under UV irradiation have also been leveraged for the degradation of organic pollutants, underscoring its promise in wastewater treatment and air purification technologies.[8] Furthermore, ZnO has emerged as one of the leading semiconductor materials in terms of radiation resistance; recent investigations – including those by two members of our research group – have explored ZnO properties following exposure to slow neutrons,[9–11] with additional studies on fast neutron irradiation underway (to be submitted soon). This exceptional radiation stability has positioned ZnO as a suitable candidate for advanced space applications.

While ZnO and SiO_2 each exhibit distinct advantages, their integration into a composite material confers notable improvements in photocatalytic performance. Embedding ZnO within a SiO_2 matrix has been shown to enhance charge separation by suppressing electron–hole recombination, thereby

[a]*Department of Physics, National Institute of Technology, Kerala, India*
[b]*Department of Mechanical and Nuclear Engineering, Khalifa University, Abu Dhabi, United Arab Emirates*
[c]*Department of Chemistry, Khalifa University, Abu Dhabi, United Arab Emirates*
[d]*Engineering Department, Higher Colleges of Technology, Abu Dhabi, United Arab Emirates*
[e]*Department of Physics, Khalifa University, Abu Dhabi, United Arab Emirates. E-mail: sufian.abedrabbo@ku.ac.ae*

improving overall photocatalytic efficiency.[12] This integration also inhibits ZnO particle aggregation, which ensures more effective light absorption and better utilization of the active photocatalyst surface.[13] Moreover, the presence of the SiO_2 matrix modifies the band structure of ZnO, extending the material's spectral response from the ultraviolet to the visible region and thus enabling efficient solar-driven photocatalysis.[14] Importantly, the SiO_2 layer significantly increases the chemical stability of ZnO, acting as a protective barrier that maintains ZnO's properties even under harsh acidic or high-temperature environments and prevents the nanoparticles from dissolving or reacting with corrosive chemicals.[15]

Beyond improvements in photocatalysis, such SiO_2 nanocomposites, when incorporated in coatings, play a vital role in tailoring optical properties for applications involving infrared (IR) and near-IR radiation of coated silicon. For instance, prior research by members of our group on sol–gel erbium-doped silica films demonstrated a substantial enhancement of infrared emission near 1.067 eV (1162 nm),[16–21] building on earlier studies concerning light emission from impurity centers in silicon.[22–26] This enhancement was attributed to interfacial stresses and strain-induced effects, which can modulate the silicon energy bandgap and mitigate non-radiative recombination losses. Similar strain-engineering mechanisms are anticipated to be operative in ZnO–SiO_2 nanocomposite-based coatings, offering avenues for tailored bandgap tuning and improved optoelectronic functionality.

The sol–gel process, whose terminology was first introduced by Graham in 1864 during his foundational studies on silica sols,[27] has become an indispensable synthesis route for oxide nanomaterials. Its practical relevance was further established when Ebelmen observed the formation of glass from silane precursors, obtained by reacting $SiCl_4$ with ethanol and exposing the resultant compound to air.[28] The present work employs this classical sol–gel strategy for nanocomposite synthesis. Despite the breadth of literature concerning sol–gel synthesis of ZnO, SiO_2, and their composites, there remains a lack of consensus on optimal processing conditions—a reality that has led to the common assertion that sol–gel synthesis is as much an art as it is a science.[29] This is largely attributable to the intricate interplay of parameters such as pH, precursor concentration, and annealing temperature, each of which exerts a pronounced effect on the resulting nanostructure, porosity, and optical response of the ZnO–SiO_2 composites.

The primary motivation for this work was to strategically design and engineer nanocomposite materials with multifunctional properties that make them attractive for a wide spectrum of energy-related applications. By engineering the composition and structure, these composites hold promise as efficient options for energy storage systems and hydrogen sorption, both of which are critical for the advancement of sustainable energy technologies. In addition to this, given the tunable surface and electronic properties such nanocomposites could also serve as highly effective photocatalysts for hydrogen production in the future. To sum up, this study not only highlights immediate challenges in energy storage and H-sorption, but also lays foundation for potential applications in renewable energy conversion, posing these materials as versatile stepping stones for next-generation energy solutions.

The overarching objective of this study is to synthesize and comprehensively characterize ZnO–SiO_2 nanocomposites *via* the sol–gel method, evaluating their structural, morphological, and optical properties relative to those of pure ZnO and SiO_2. It is observed that sol–gel derived nanostructures cannot always match the performance of other advanced deposition techniques in devices with higher integration. However, the sol–gel route offers distinct advantages in terms of low-cost processing, scalability for mass production and compositional tunability of nanostructured oxides. These features make it particularly apt for large-area coatings, photocatalysis, and for engineering nanocomposites from transitional metals that enjoy high density of pores and affinity for hydrogen, and other application domains where economic and scalable fabrication is prioritized. By optimizing the sol–gel conditions, this work aims to advance the rational design of ZnO–SiO_2 nanocomposites for promising future applications, including hydrogen storage and optoelectronic device integration.

2. Experimental procedure

2.1 Synthesis of silica (SiO_2)

Acetic acid was selected as the pH-controlling agent for silica synthesis in preference to hydrochloric acid, owing to its capacity to reduce defect density and promote more controlled polycondensation, ultimately enhancing the structural integrity of the final SiO_2 material.[30,31] To ensure optimal miscibility and prevent premature gelation, an ethanol-to-TEOS (tetraethyl orthosilicate) ratio of 10 : 1 was maintained, facilitating a uniform sol–gel transition.[32] The thermal treatment regime was carefully staged, beginning with gelation at 75 °C, followed by drying at 120 °C, and concluding with annealing in the 700–900 °C range, a sequence that was designed to minimize structural collapse as depicted from ref. 33 and 34.

The synthesis protocol employed a TEOS : EtOH : H_2O molar ratio of 1 : 10 : 4, with acetic acid (0.05 mol per mol TEOS) acting as the catalyst. This combination was selected based on Fardad's work, which demonstrated that low water content and acetic acid catalysis favor the formation of mesoporous structures while minimizing microcrack formation.[30] Ethanol functioned dually as a solvent and homogenizing agent, effectively preventing phase separation between TEOS and water during hydrolysis.[32] Following vigorous stirring at 300 rpm for 3 hours at 25 °C, gelation was initiated at 75 °C – a critical step for achieving uniform pore distribution.[33] An ageing period of 18 hours allowed the Si–O–Si network to strengthen *via* Ostwald ripening.[35] Subsequent annealing at higher temperatures (up to 900 °C) resulted in densification, albeit with a reduction in surface area, consistent with behavior observed in SiO_2–ZnO composites.[31]

2.2 Synthesis of zinc oxide (ZnO)

The synthesis of ZnO nanoparticles was informed by prior optimization studies. Zinc acetate was chosen as the precursor,

as it reliably yields smoother surfaces compared to nitrate-based alternatives.[36] A sodium hydroxide concentration of 1 M was used to balance nucleation rate and aspect ratio, favoring controlled growth of nanorods.[37] The final annealing temperature was set at 450 °C, optimizing crystallinity while mitigating excessive grain growth.[38]

ZnO nanoparticles were precipitated from a solution of zinc acetate dihydrate (10 g in 100 mL ethanol) *via* the gradual addition of 1 M NaOH. This approach aligns with Hasnidawani *et al.*, who demonstrated that ethanol enables the controlled nucleation of rod-like ZnO structures.[39] The lower polarity of ethanol compared to water slows the formation of hydroxide ions, promoting oriented growth along the (002) planes.[40] A 24-hour aging step ensured complete formation of zinc hydroxide, with accordance with a study conducted by Alias *et al.* that confirmed that any zinc hydroxide left would be decomposed to zinc oxide (ZnO) and water (H_2O).[41] Subsequent thermal decomposition at 450 °C effectively removed residual acetate, yielding crystallites smaller than 50 nm—dimensions suitable for sol–gel-based photoelectrochemical applications.[42]

2.3 Synthesis of ZnO–SiO_2 nanocomposite

For the composite synthesis, a ZnO loading of 10% (by weight). Studies showed that a 10% wt ZnO composite with silica was seen to be characterized with largest specific surface area, in comparison to a 5% wt ZnO and 20% wt ZnO composite.[43] This could indicate an increase in physisorption states, which could be favorable for hydrogen storage. Hydrochloric acid at a concentration of 0.03 M was introduced to prevent the undesirable precipitation of $Zn(OH)_2$, thus preserving compositional homogeneity.[44] A layered annealing protocol, spanning 700–900 °C, was employed to mitigate interfacial thermal stress and reinforce structural integrity.[33]

The composite (10 : 90 $ZnO : SiO_2$) was prepared by combining TEOS hydrolysis (using HCl as catalyst) with subsequent incorporation of the zinc acetate precursor. The acidic environment established by HCl not only accelerated TEOS polycondensation but also facilitated effective Zn^{2+} dispersion within the silica matrix.[31] Sequential addition—beginning with TEOS, followed by HCl/water and then the Zn precursor—was implemented in accordance with the G4 methodology proposed by Mocioiu *et al.* ref. 31. The resulting mixture was stirred at 500 rpm for 30 minutes, achieving homogeneity without disrupting Si–O–Zn bonding.[34] An 18-hour aging step enabled Zn^{2+} ions to diffuse into the SiO_2 matrix pores,[45] while subsequent annealing further enhanced interfacial bonding.[46,47]

2.4 Characterization techniques

The structural and morphological features of the synthesized powders were systematically characterized. X-ray diffraction (XRD) analyses were performed using a Bruker D2 Phaser diffractometer with CuKα_1 radiation ($\lambda = 1.54$ nm) to determine crystallographic phases. Complementary characterization methods included Fourier transform infrared (FTIR) spectroscopy (Bruker-ALPHA, 400–4000 cm^{-1}) for the identification of functional groups, and scanning electron microscopy (SEM) paired with energy-dispersive X-ray spectroscopy (EDS) for detailed investigation of surface morphology and elemental distribution (FEI Quanta FEG 250 with EDAX EDS Detector).

3. Results and discussion

3.1 X-ray diffraction analysis

The crystalline nature, phase composition, and thermal behavior of the synthesized powders were systematically investigated using XRD performed on pure SiO_2, ZnO, and ZnO–SiO_2 composites, both in their as-synthesized state and after thermal annealing at 700 °C, 800 °C, and 900 °C. The resulting diffraction profiles were processed and visualized using OriginPro. As shown in Fig. 1, the XRD patterns for SiO_2 exhibited broad, diffuse features indicative of its amorphous structure, with negligible peak definition across all annealing temperatures (700–900 °C). A slight sharpening of the amorphous halo was observed with increasing temperature. However, in the sample annealed at 900 °C, we see a sharp peak at 27°. This can be attributed to the peak observed for the (101) plane of crystalline α-quartz.[48,49] Apart from this peak, the sample remains mostly amorphous, that aligns with extensive literature reports, which indicate that sol–gel-derived SiO_2 typically maintains its amorphous character up to temperatures as high as 1000 °C.[50]

In contrast, the XRD pattern of the synthesized ZnO, as demonstrated in Fig. 2, confirmed the formation of a crystalline structure in the hexagonal wurtzite phase, consistent with established reference standards. The notable broadening at the FWHM of the diffraction lines across the ZnO patterns is indicative of nanometer-scale crystallites. Characteristic peaks observed at 32.2°, 34.85°, 36.7°, 47.9°, 57.0°, 63.2°, 66.9°, 68.3°, 69.5°, 73.1°, and 77.3° can be indexed to the (100), (002), (101), (102), (110), (103), (200), (112), (201), (004), and (202) planes of ZnO, respectively.[51] The average crystallite size of ZnO nanoparticles, as calculated using the Scherrer equation, $D = \frac{K\lambda}{\beta \cos \theta}$ was determined to be approximately 18.4 nm. In other literature, following a similar sol gel process, average

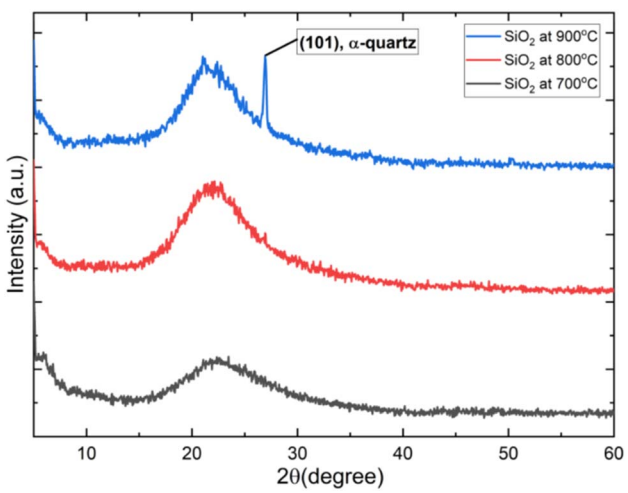

Fig. 1 XRD pattern for SiO_2 at different annealing temperatures.

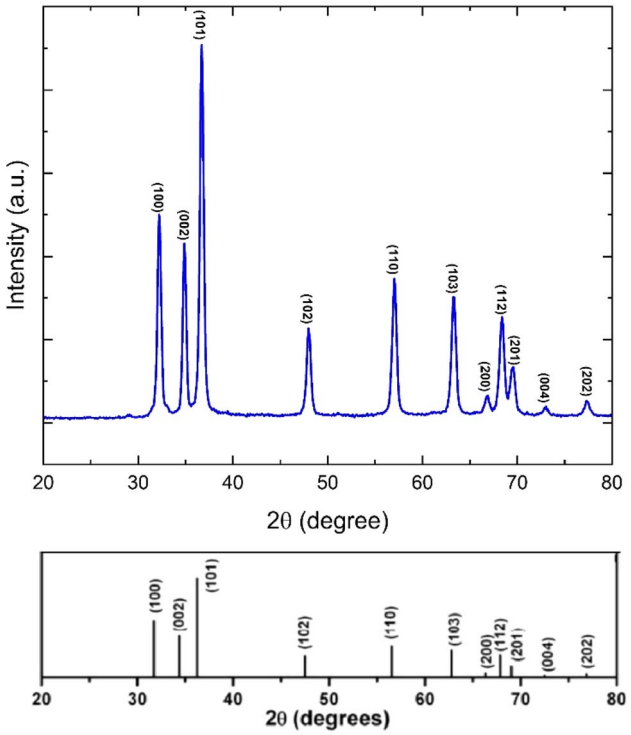

Fig. 2 XRD patterns for ZnO annealed at 450 °C (top) as compared to standard XRD data for ZnO (bottom).

crystallite size of about 21 nm is seen.[52] We were able to achieve a slightly lesser crystallite size *via* our mode of synthesis.

Fig. 3 presents the XRD patterns of the SiO_2–ZnO composite, both as-synthesized and following annealing at 700 °C, 800 °C, and 900 °C. This observation indicates that the composite is predominantly composed of an amorphous silica matrix, with ZnO present in either a highly disordered or nanocrystalline state, consistent with the low ZnO loading ($ZnO : SiO_2 = 10 : 90$).[53]

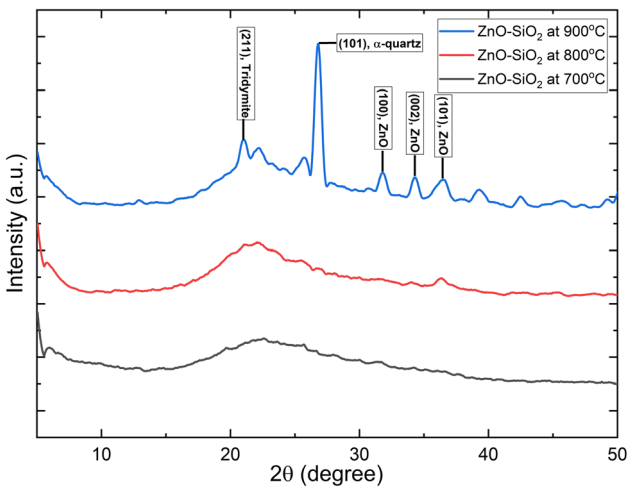

Fig. 3 XRD pattern for ZnO–SiO_2 composite at different annealing temperatures.

Upon annealing at 700 °C (black curve), there is a subtle sharpening of the background, yet no distinct peaks emerge, suggesting that the material remains largely amorphous at this temperature. Any possible ZnO crystallites are presumably too small or insufficiently ordered to yield detectable diffraction features—an effect attributable to both the low ZnO content and the encapsulating amorphous SiO_2 matrix. At 800 °C (red curve), the XRD pattern exhibits a similar profile; while the incipient formation of minor peaks is noted, their intensity remains too weak for reliable assessment, indicating only marginal increases in crystallinity.

The most significant transformation occurs upon annealing at 900 °C (blue curve), where weak but clearly discernible diffraction peaks begin to emerge from the amorphous background. Notably, peaks at $2\theta = 31.7°$, 34.4°, and 36.2° correspond to the (100), (002), and (101) planes of the hexagonal wurtzite ZnO phase.[54] The enhancement in peak intensity and reduction in full width at half maximum (FWHM) are indicative of improved crystallinity and grain growth. These peaks are, however, seen to be shared by both ZnO, as well as $ZnSiO_4$. Therefore, there is a possibility for the formation of silicates in the composite. The peak in the SiO_2 annealed at 900 °C, is again observed here, which corresponds to the crystalline α-quartz. Along with this, we see a peak at ~21°, which corresponds to the (211) plane of tridymite. However, tridymite is only seen at annealing temperatures above 870 °C. In a study conducted by Lee *et al.*, ZnO, being an intermediate metal oxide, is known to serve as a network former/enhancer, that has the ability to enhance bonds in a silica matrix, thereby promoting crystallization.[55] Thereby, we observe a promotion of crystallization by ZnO, thereby leading to the formation of tridymite in the composite.

3.2 FTIR analysis

The FTIR transmittance spectra, as observed by Fig. 4a, recorded in the range of 400 to 4000 cm^{-1}, confirm the successful synthesis of SiO_2 nanoparticles. Across all three annealing temperatures, a strong band at 803 cm^{-1} and 1064 cm^{-1} is consistently observed and attributed to the symmetric and asymmetric stretching vibrations of the Si–O–Si bonds.[56] A peak is also observed at 453 cm^{-1}, which is attributed to the bending vibrations of Si–O–Si bonds.[57] The FTIR spectrum of the synthesized ZnO sample is depicted in Fig. 4b. Peaks below 500 cm^{-1} are indicative the presence of ZnO and corresponds to the Zn–O stretching vibrations. We observe a characteristic vibrational stretching at 461 cm^{-1}, which matches with the ref. 58 and.[59] The peak near 861 cm^{-1} confirms the presence of Zn–O in the sample.[60] Beyond this region, the baseline of the spectrum is relatively flat up to 4500 cm^{-1}, with only minor features. A subtle undulation around 2340 cm^{-1} is attributed to atmospheric CO_2 detected during measurement—a common artifact in FTIR analyses and not intrinsic to the material.[61]

Fig. 4c presents the FTIR spectra of the ZnO–SiO_2 nanocomposite, obtained after calcination at 700 °C, 800 °C, and 900 °C. These spectra reveal both temperature-dependent trends and the distinct fingerprints of the composite's

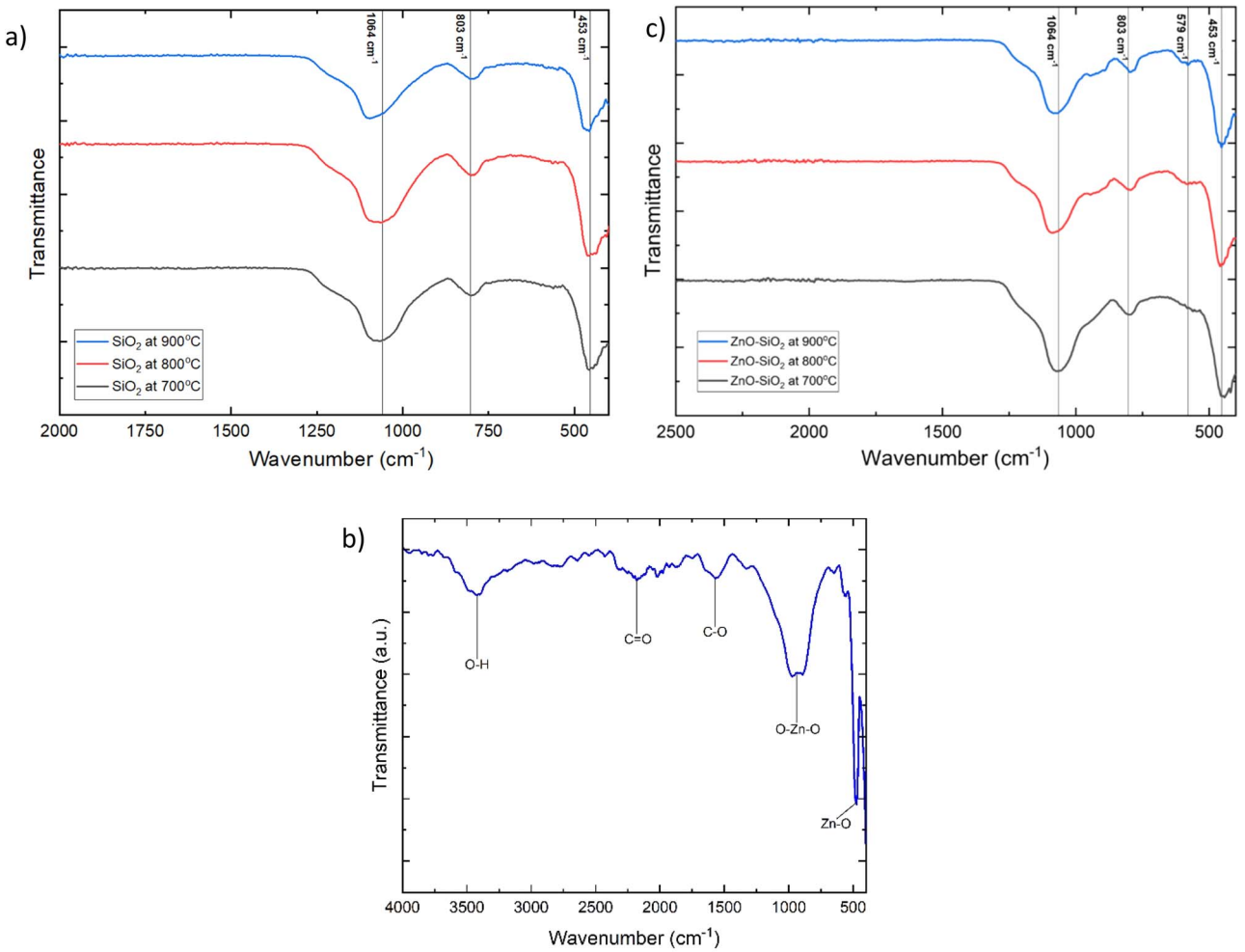

Fig. 4 FTIR spectra for (a) SiO_2 at 700 °C, 800 °C and 900 °C (b) ZnO at 450 °C (c) ZnO–SiO_2 composite at 700 °C, 800 °C and 900 °C.

components. Sharp peaks centered at approximately 803 cm^{-1} and 1064 cm^{-1} are definitively assigned to the asymmetric stretching vibrations of Si–O–Si bonds, as seen in the case of SiO_2. The sharp peak at 453 cm^{-1} attributes to the bending vibrations of Si–O–Si bonds.[57] At the wavenumber 579 cm^{-1}, a smaller absorption peak emerges and becomes increasingly defined with rising annealing temperature. This feature is likely associated with the formation of Si–O–Zn bonds, supporting the temperature-induced evolution of the composite interface. These spectral signatures are consistent with prior FTIR studies reported in the literature.[14,62,63]

An increase in the absorption intensity (corresponding to a decrease in transmission intensity) is observed in the ZnO–SiO_2 intensity. This is shown in Fig. 5 by isolating the sharp peak at the 1070–1100 cm^{-1} range. On normalization, A 46.71% increase is observed in the absorption intensity when ZnO is introduced. This can be attributed to the enhanced vibrational dipole activity due to the incorporation of Zn. Formation of the Si–O–Zn bonds, leads to a localized asymmetry, thereby causing a perturbation in the bond polarities within the silicate network, hence increasing the change in effective dipole moment during vibrational transitions. Since, IR absorption strength increases when change in dipole moment increases

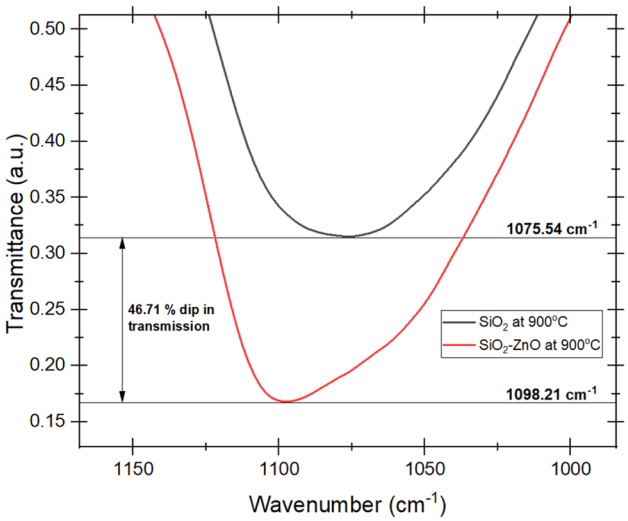

Fig. 5 Increase in absorption intensity on incorporation of Zn into the SiO_2 matrix.

$(\partial\mu/\partial q)$, this structural addition leads to more intense absorption bands, thereby resulting in an increase in absorption intensity.[64]

3.3 SEM-EDS analysis

As illustrated in Fig. 6a, SEM was employed to investigate the surface morphology of the synthesized nanoparticles, while EDS mapping was utilized to assess the spatial distribution of constituent elements. SEM images were acquired in secondary electron mode at accelerating voltages of 5 kV, 10 kV, and 20 kV, with spot sizes of 2.5 and 3.5 adjusted according to sample requirements. Elemental mapping was performed under the same operating conditions to ensure consistent spatial resolution.

At 700 °C, the silica particles exhibited relatively smooth, amorphous surfaces with minimal textural features. Upon increasing the annealing temperature to 800 °C, the particles began to adopt more defined shapes with sharper edges, indicative of enhanced condensation and structural reorganization within the silica network. The most pronounced morphological transformation occurred at 900 °C, where the formation of highly agglomerated structures became evident. At this temperature, the sample displayed clusters composed of smaller, well-defined particles coalescing into larger aggregates. This agglomeration is likely driven by increased particle mobility and elevated surface energy at high temperatures, facilitating the fusion of smaller domains into more thermodynamically stable, larger clusters.

EDS analysis (Fig. 6b) consistently confirmed a homogeneous distribution of silicon and oxygen throughout all samples, with elemental spectra matching the expected stoichiometry of SiO_2. The particles predominantly exhibited formation of agglomerates, characteristic of amorphous silica synthesized *via* sol–gel methods. We see a minor carbon peak at ~0.28 keV in the EDS spectrum. This could be due to residual organics that were not fully removed on annealing. However, the probability for this to be the reason is quite low as no blackening of the sample was observed. Hence, it is highly suspected to be because of re-adsorption of organic compounds from the ambient environment into the sample.

The SEM image presented in Fig. 7a illustrates the morphological features of ZnO nanoparticles annealed at 450 °C. The sample reveals a hierarchical, three-dimensional architecture composed of highly clustered, flower-like agglomerates, with branching structures radiating from central nucleation sites. This complex morphology is attributed to the elevated annealing temperature, which supplies the required thermal energy to promote substantial crystallite growth and the formation of intricate assemblies.[65] The EDS spectrum (Fig. 7b) provides definitive evidence for the elemental composition of the ZnO sample, with pronounced peaks corresponding to zinc and oxygen. The Zn Kα peak appears at approximately 1.1 keV, while the oxygen signal is observed near 0.5 keV, confirming the expected stoichiometry.

Surface morphology changes significantly when annealing the ZnO–SiO_2 nanocomposite at progressively higher temperatures (700, 800 and 900 °C). The composite preserves the angular, blocky shards typical of the as-deposited sol–gel precursor at 700 °C (Fig. 8a); these fragments show sharp edges and strong surface roughness. Increasing the temperature to 800 °C (Fig. 8b) starts particle coalescence and facet smoothing: small particulates fuse, producing larger domains with less high-curvature features, consistent with the start of silica softening and viscous flow in the network. Extensive grain growth and densification have occurred by 900 °C (Fig. 8c). Embedded in a glassy SiO_2 matrix that has softened enough to round off particle corners (indicating enhanced crystallization and particle growth)[66] and heal minor surface defects are individual ZnO crystals. This high-temperature microstructure shows occasional micro-cracks most likely resulting from differential thermal expansion between the ZnO phase and the surrounding silica.

The EDS elemental analysis at 900 °C (Fig. 8d) only shows the signature peaks of silicon (Si Kα, ~1.74 keV), zinc (Zn Lα, ~1.01 keV), and oxygen (O Kα, ~0.52 keV). This confirms that the composite is free of adventitious contamination and that both ZnO and SiO_2 phases are still present. A homogeneous ZnO–

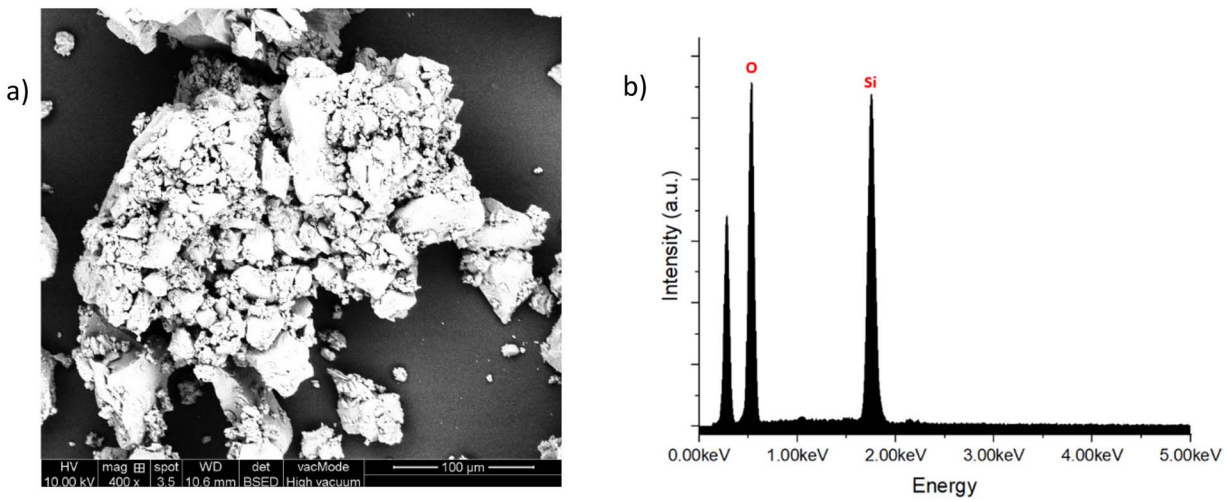

Fig. 6 (a) SEM image of SiO_2 annealed 900 °C (b) EDS mapping of SiO_2 annealed at 900 °C.

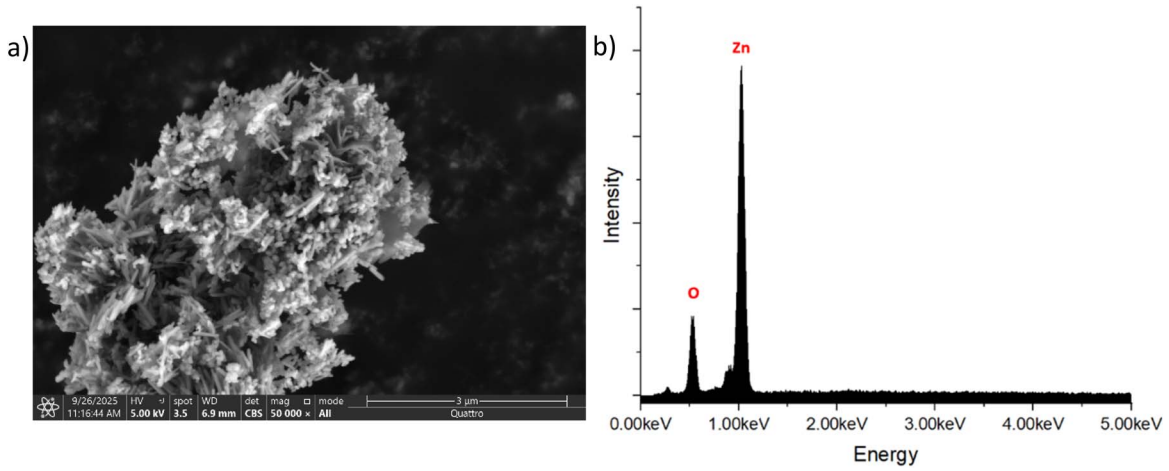

Fig. 7 (a)SEM image of ZnO at annealing temperature 450 °C, (b) EDS mapping of ZnO at annealing temperature 450 °C.

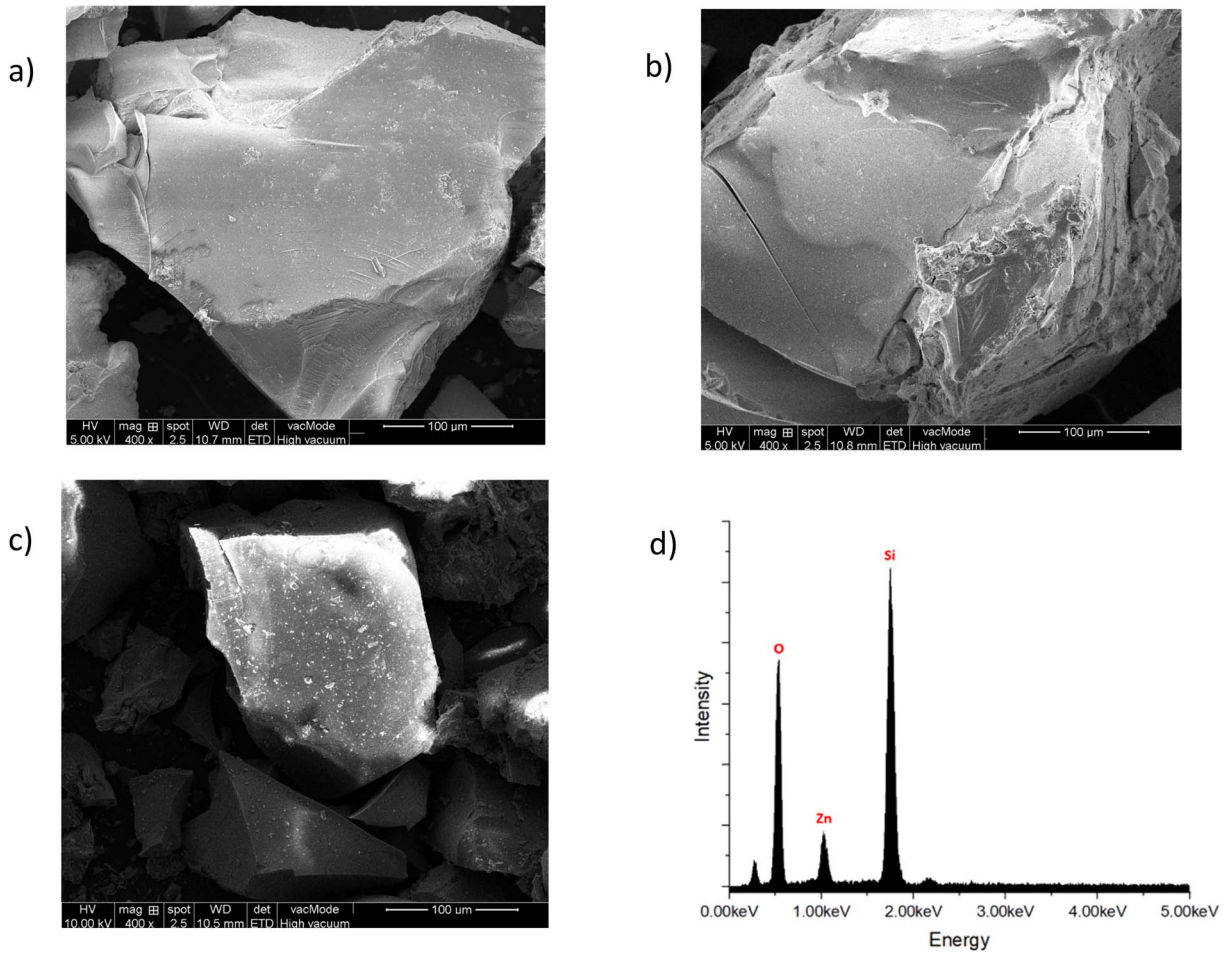

Fig. 8 SEM images of ZnO–SiO_2 composite at annealing temperatures (a) 700 °C, (b) 800 °C and (c) 900 °C (d) EDS spectrum of composite annealed at 900 °C. (d) EDS mapping of ZnO–SiO_2 nanocomposite 900 °C.

SiO_2 matrix with no discernible residual carbon or other impurities is qualitatively consistent with the relative intensities of the O, Zn, and Si signals. When combined, these findings show that annealing at 900 °C causes the structural relaxation and coarsening required to create a dense, polycrystalline ZnO–SiO_2 composite in addition to completely burning organic residues from the TEOS/acetic-acid sol–gel process.

EDS elemental mapping (Fig. 9) reveals the spatial distribution of Zn, Si and O in the composite. Each mapping image was obtained from independent energy windows corresponding to

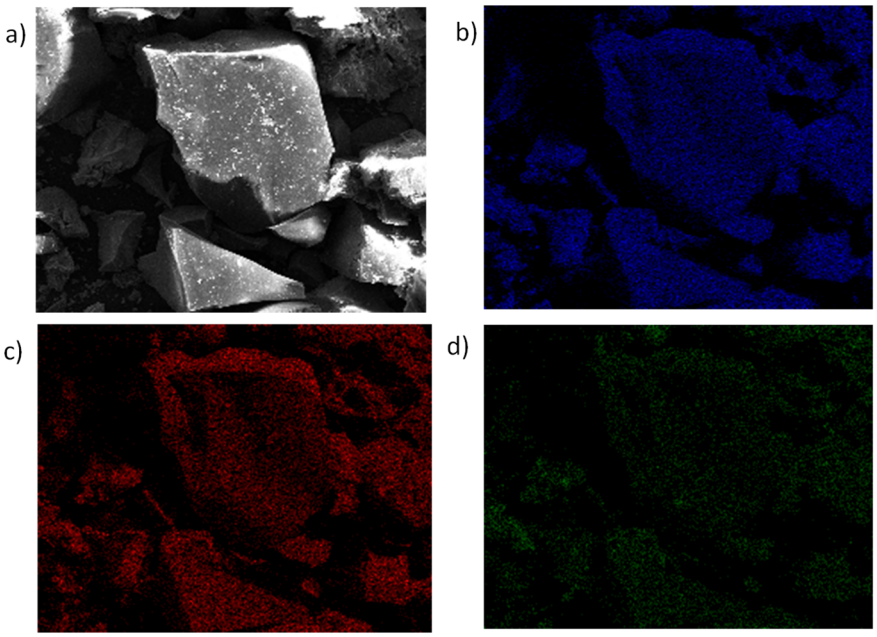

Fig. 9 Elemental mapping for SiO_2–ZnO composite annealed at 900 °C (a) the sample itself (b) Si (c) O (d) Zn.

the characteristic X-ray emission lines of the respective elements, and the differences in spatial intensity clearly show the distribution of elements across the sample. From the maps, we see a homogenous distribution of Si and O, implying a consistent SiO_2 matrix. However, the Zn seems to be sparse and unevenly distributed. This lies in agreement with the 90 : 10 ratio of SiO_2–ZnO. The faint Zn signals suggest that the ZnO is combined in the matrix *via* interfacial bonding rather than existing as a separate phase, thereby in agreement with the peak at 579 cm^{-1} in the FTIR results. This complementary distribution, consistent with the composite structure, provides strong evidence that the maps represent genuine elemental distributions. However, it is worth noting that EDS, while being powerful in computing surface compositional analysis, is limited in its ability to capture trace elements like Zn in a dominant SiO_2.

While EDS mapping has provided useful insights into elemental distribution, its limited sensitivity to trace Zn signals suggests scope for further refinement. In our future studies we intend to employ complementary techniques such as TEM-EDS or XPS to achieve higher sensitivity and spatial resolution, thereby offering a more detailed understanding of Zn distribution.

4. Conclusion

In this study, we have successfully synthesized SiO_2, ZnO, and SiO_2–ZnO (90 : 10) nanocomposite powders *via* a tailored sol–gel method, with particular emphasis on controlled hydrolysis and aging processes and effect of thermal treatment. Comprehensive characterization using XRD, FT-IR, and EDS enabled a detailed investigation of the structural and interfacial properties of these materials as a function of annealing temperature. X-ray diffraction analysis confirmed the persistence of an amorphous silica matrix alongside the development of nanocrystalline wurtzite ZnO domains within the composite upon thermal treatment. FT-IR spectroscopy revealed the presence of both Zn–O stretching vibrations and Si–O–Si asymmetric modes, while comparative analysis with literature further indicated the formation of Zn–O–Si bonds (notably at 579 cm^{-1}), signifying chemical interaction at the ZnO–SiO_2 interface.

Elemental mapping by EDS demonstrated a homogeneous distribution of silicon, zinc, and oxygen, evidencing the successful and coherent integration of ZnO within the silica matrix. The retention of structural homogeneity and the formation of robust interfacial bonds underscore the efficacy of the adopted sol–gel synthesis approach. Collectively, these findings establish a foundational understanding of the morphological evolution and interfacial chemistry in SiO_2–ZnO nanocomposites, thereby providing a platform for future investigations aimed at tailoring these materials for advanced applications in catalysis, optoelectronics, and environmental remediation.

While EDS mapping has provided useful insights into elemental distribution, its limited sensitivity to trace Zn signals suggests scope for further refinement. Future studies could employ complementary techniques such as TEM-EDS or XPS to achieve higher sensitivity and spatial resolution, thereby offering a more detailed understanding of Zn distribution.

This work proved the ability to achieve low-cost synthesis of various dielectric nanocomposites and to perform comparative studies that indicated the grain growth promoting effect of ZnO on SiO_2 as well as the ability to engineer ultrasmall granules of ZnO that naturally possess large surface area for future applications of gas adsorption as both sensors and possible energy

storing candidate in addition to possible photocatalytic applications.

Conflicts of interest

Authors declare that there is no conflict of interest.

Data availability

Data included in the figures and tables are available in the following link: **https://drive.google.com/drive/folders/1pASLOubX7Kx-3avMt62KLI9dR6qz6ls9?usp=sharing**.

Supplementary information is available. See DOI: **https://doi.org/10.1039/d5na00612k**.

Acknowledgements

We would like to express our appreciation to the chemistry department in Khalifa University for availing their laboratories. The authors would like to acknowledge Khalifa University HR for enrolling Allen Samuel as research visitor for summer of 2024 and for Samuel Stephen for technical discussion.

References

1 Z. Ahmed, L. S. Nasrat and M. Rihan, The effect of SiO2 microparticle concentration on the electrical and thermal properties of silicone rubber for electrical insulation applications, *Electr. Eng. Electromechanics*, 2025, **3**, 84–89.
2 P. S. Shinde, P. S. Suryawanshi, K. K. patil, V. M. Belakar, S. A. Sankpal, S. D. Delekar and S. A. Jadhav, A Brief Overview of Recent Progress in Porous Silica as Catalyst Supports, *J. Compos. Sci.*, 2021, **5**(3), 75.
3 A. Pallares-García, J. L. Contreras, J. Pérez-Cabrera, B. Zeifert, T. Vázquez, J. Salmones and M. A. Gutiérrez-Limón, Stabilization of Pt in SiO_2–Al_2O_3 Microspheres at High Mechanical Resistance, Promoted with W Oxides for the Combustion of CO, *Catalysts*, 2021, **11**(11), 1320.
4 C. Roßkopf, M. Gollsch, A. Faik, M. Linder and A. Wörner, Improving Powder Bed Properties for Thermochemical Storage by Adding Nanoparticles, *Energy Convers. Manage.*, 2014, **86**, 93–98.
5 D. K. Sharma, S. Shukla, K. K. Sharma and V. Kumar, A review on ZnO: Fundamental properties and applications, *Mater. Today: Proc.*, 2022, **49**(8), 3028–3035.
6 S. Dhall, B. R. Mehta, A. K. Tyagi and K. Sood, A review on environmental gas sensors: Materials and technologies, *Sens. Int.*, 2021, **2**, 100116.
7 N. Babayevska, L. Przysiecka, I. Iatsunskyi, G. Nowaczyk, M. Jarek, E. Janiszewska and S. Jurga, ZnO size and shape effect on antibacterial activity and cytotoxicity profile, *Sci. Rep.*, 2022, **12**(1), 8148.
8 A. Baig, S. Mohsin and P. Sandeep, A Review of Visible-Light-Active Zinc Oxide Photocatalysts for Environmental Application, *Catalysts*, 2025, **15**(2), 100.
9 M. M. Zeidan and S. Abedrabbo, Enhancing photoluminescence spectra for doped ZnO using neutron irradiation, *ACS Omega*, 2023, **8**, 16722–16728.
10 M. M. Zeidan and S. Abedrabbo, Neutron irradiation to transmute zinc into gallium, *Nanomaterials*, 2023, **13**, 1487.
11 M. M. Zeidan, A. Abdullah and S. Abedrabbo, Formation of GdAl2 laves phase in gadolinium zinc oxide epitaxy film, *JOM*, 2024, **75**(9), 3612–3619.
12 X. Shen, Y. Shi, H. Shao, Y. Liu and Y. Zhai, Synthesis and photocatalytic degradation ability evaluation for rhodamine B of ZnO@SiO_2 composite with flower-like structure, *Water Sci. Technol.*, 2019, **80**(10), 1986–1995.
13 J. Huang, G. Fei, S. Xu and B. Wang, ZnO–SiO_2 composite coating with anti-reflection and photoluminescence properties for improving the solar cell efficiency, *Composites, Part B*, 2022, **251**, 110486.
14 A. Dhaffouli, M. Holzinger, S. Carinelli, H. Barhoumi and P. A. Salazar-Carballo, ZnO Doped Silica Nanoparticles (ZnO@SiO_2) for Enhanced Electrochemical Detection of Cd^{2+} Ions in Real Samples, *Sensors*, 2024, **24**(13), 4179.
15 M. A. Alam, U. A. Samad, A. Anis, M. Alam, M. Ubaidullah and S. M. Al-Zaharani, Effects of SiO2 and ZnO Nanoparticles on Epoxy Coatings and Its Performance Investigation Using Thermal and Nanoindentation Technique, *Polymers*, 2021, **13**(9), 1490.
16 A. Abdullah, E. M. Benchafia, D. Choi and S. Abedrabbo, Synthesis and Characterization of Erbium-Doped Silica Films Obtained by an Acid–Base-Catalyzed Sol–Gel Process, *Nanomaterials*, 2023, **13**(9), 1508.
17 S. Abedrabbo, A. T. Fiory and N. M. Ravindra, Engineered stresses for a functional Si light emitter at bandgap: An overview, *JOM*, 2019, **71**(12), 4857–4866.
18 S. Abedrabbo, A. T. Fiory and N. M. Ravindra, Evidence of silicon band-edge emission enhancement when interfaced with SiO_2:Er films, *JOM*, 2017, **69**, 241–246.
19 S. Abedrabbo, A. T. Fiory and N. M. Ravindra, Processing for highly emissive Cz-silicon by depositing stressed sol-gel films, *JOM*, 2014, **66**, 643–648.
20 S. Abedrabbo, B. Lahlouh, S. Shet and A. T. Fiory, Room-temperature silicon band-edge photoluminescence enhanced by spin-coated sol-gel films, *Scr. Mater.*, 2011, **65**(9), 767–770.
21 S. Abedrabbo, B. Lahlouh and A. T. Fiory, Analytical study of thermal annealing behaviour of erbium emission in Er_2O_3-sol-gel silica films, *J. Phys. D: Appl. Phys.*, 2011, **44**, 509901.
22 S. Abedrabbo, M. M. Zeidan, A. Abdullah, I. A. Qattan, J. Hassan and A. T. Fiory, Formation of Si-Er-O structures in Si by Ar-irradiation for harvesting light at the 4d intraband transition, *Radiat. Phys. Chem.*, 2025, **231**, 112607.
23 S. Abedrabbo, Q. Mohammed and A. T. Fiory, Processing for optically active erbium in silicon by film co-deposition and ion-beam mixing, *Appl. Surf. Sci.*, 2009, **255**(8), 4503–4511.
24 S. Abedrabbo and A. T. Fiory, Ambient erbium luminescence in silicon and silicon-germanium films, *Emerging Mater. Res.*, 2012, **1**, 17–24.

25 S. Abedrabbo, D. E. Arafah and S. Salem, Ion beam mixing of silicon-germanium thin films, *J. Electron. Mater.*, 2005, **34**, 468–473.
26 S. Abedrabbo, D. E. Arafah, O. Gokce, L. S. Wielunski, M. Gharaibeh, O. Celik and N. M. Ravindra, Ion beam mixing for processing of nanostructure materials, *J. Electron. Mater.*, 2006, **35**, 834–839.
27 T. Graham, XXXV. – On the properties of silicic acid and other analogous colloidal substances, *J. Chem. Soc.*, 1864, (17), 318–327.
28 J. D. Wright, and N. A. J. M. Sommerdijk, *Sol-gel Materials: Chemistry and Applications*. CRC Press, 2018.
29 D. Navas, S. Fuentes, A. Castro-Alvarez and E. Chavez-Angel, Review on Sol-Gel Synthesis of Perovskite and Oxide Nanomaterials, 2021, *Gels*, 2021, **7**(4), 275.
30 M. A. Fardad, Catalysts and the Structure of SiO_2 Sol-Gel Films, *J. Mater. Sci.*, 2000, **35**, 1835–1841.
31 O.-C. Mocioiu, C. M. Vladut, I. Atkinson, V. Bratan and A.-M. Mocioiu, The Influence of Gel Preparation and Thermal Treatment on the Optical Properties of SiO_2–ZnO Powders, *Gels*, 2022, **8**, 242.
32 C. J. Brinker, and G. W. Scherer, *Sol-Gel Science: the Physics and Chemistry of Sol-Gel Processing*, Academic Press: Boston, 1990.
33 J. Livage and M. H. C. Sanchez, Sol-Gel Chemistry of Transition Metal Oxides, *Prog. Solid State Chem.*, 1988, **18**, 259–341.
34 L. L. Hench and J. K. West, The Sol-Gel Process, *Chem. Rev.*, 1990, **90**, 33–72.
35 O. P. Konuk, A. A. A. M. Alsuhile, H. Yousefzadeh, Z. Ulker, S. E. Bozbag, C. A. Garcia-Gonzalez, I. Smirnova and C. Erkey, The effect of synthesis conditions and process parameters on aerogel properties, *Front. Chem.*, 2023, **11**, 1294520.
36 S. Kaenphakdee, P. Putthithanas, S. Yodyingyong, J. Leelawattanachai, W. Triampo, N. Sanpo, J. Jitputti and D. Triampo, Zinc Oxide Synthesis from Extreme Ratios of Zinc Acetate and Zinc Nitrate: Synergistic Morphology, *Materials*, 2022, **15**(2), 570.
37 V. Koutu, L. Shastri and M. M. Malik, Effect of NaOH concentration on optical properties of zinc oxide nanoparticles, 2016, *Mater. Sci.*, 2016, **4**, 819–827.
38 A. Abdel-Galil, M. S. A Hussien and M. R. Balboul, Optimal thickness and annealing temperature for enhancement of structural, optical, and photocatalytic properties of ZnO thin films, *J. Aust. Ceram. Soc.*, 2022, **58**, 1667–1683.
39 J. N. Hasnidawani, H. N. Azlina, H. Norita, N. N. Bonnia, S. Ratim and E. S. Ali, Synthesis of ZnO Nanostructures Using Sol-Gel Method, *Procedia Chem.*, 2016, **19**, 211–216.
40 G. Wang, X. Bao, X. Wang, X. Chen, W. Lai, D. Wu, C. Zhang, L. Gao, M. Cao, X. Li, Q. Wang, H. Wang, C. Zhang, Y. Ma and H. Wan, Preferred crystal plane growth orientation induced by low-energy ions for highly reversible zinc anodes, *Chem. Eng. J.*, 2025, **509**, 161391.
41 S. S. Alias, and A. A. Mohamad, *Synthesis of Zinc Oxide by Sol-Gel Method for Photoelectrochemical Cells*, Springer Briefs, 2014.
42 S. F. Hasany, S. Hussain, S. M. U. Ali, W. Abdul-Kadhim and M. Amir, ZnO nanostructures : comparative synthetic and characterisation studies, *Micro Nano Lett.*, 2020, **15**, 972–976.
43 B. Eren, M. K. Gunduz, G. Kaymak, D. Berikten and Z. B. Bahsi, Therapeutic Potential of Sol–Gel ZnO Nanocrystals: Anticancer, Antioxidant, and Antimicrobial Tri-Action, *ACS Omega*, 2024, **9**(13), 14818–14829.
44 S.-Y. Wang, J.-Y. Ma, Z.-J. Li, N. R. Alkurd, W.-L. Zhou, L. Wang, B. Du and Y.-L. Tang, Surface acoustic wave ammonia sensor based on ZnO/SiO2 composite film, *J. Hazard. Mater.*, 2015, **285**, 368–374.
45 R. M. S. Martins, V. Musat, A. Mücklich, N. Franco and E. Fortunato, Characterization of mesoporous ZnO:SiO_2 films obtained by the sol–gel method, *Thin Solid Films*, 2010, **518**, 7002–7006.
46 Z. Z. Zhi, Y. Qi, H. Z. Yang, J. H. Wang, X. M. Yu and B. S. Zhang, Effects of annealing temperature on optical properties of ZnO nanocrystals embedded in SiO_2 matrix thin films, *J. Phys. D: Appl. Phys.*, 2007, **40**, 4281.
47 T. N. Koltunowicz, K. Czarnacka, P. Galaszkiewicz, F. F. Komarow, M. A. Makhavikou and O. V. Milchanin, Influence of Annealing on the Dielectric Properties of Zn-SiO2/Si Nanocomposites Obtained in "Hot" Implantation Conditions, *Nanomaterials*, 2022, **12**(19), 3449.
48 A. R. Aidid, M. K. H. Shishir, M. A. Rahaman, M. T. Islam, M. Mukta and M. A. Alam, Powder X-ray line diffraction pattern profiling of anatase-quartz binary oxide: A crystallographic investigation, *Next Mater.*, 2025, **8**, 100571.
49 R.-F. Zuo, G.-X. Du, W.-G. Yang, L.-B. Liao and Z. Li, Mineralogical and chemical characteristics of a powder and purified quartz from Yunnan Province, *Open Geosci.*, 2016, **8**(1), 606–611.
50 M. Lederer, A. Reck, K. Mertens, R. Olivo, P. Bagul, A. Kia, B. Volkmann, T. Kämpfe, K. Seidel and L. M. Eng, Impact of the SiO_2 interface layer on the crystallographic texture of ferroelectric hafnium oxide, *Appl. Phys. Lett.*, 2021, **118**(1), 012901.
51 M. Abdel-Rahman, H. Ibrahim, M. Y. A. Mostafa, M. A. Abdel-Rahman, M. R. Ebied and E. A. Badawi, The characterization of ZnO nanoparticles by applying x-ray diffraction and different methods of peak profile analysis, *Phys. Scr.*, 2021, **96**(9), 095704.
52 M. T. Thein, J. Chim, S. Pung and Y. F. Pung, Highly UV light driven WO_x@ZnO nanocomposites synthesized by liquid impregnation method, *J. Ind. Eng. Chem.*, 2017, **46**, 119–129.
53 M. Hessien, E. Da'na, K. AL-Amer and M. M. Khalaf, Nano ZnO (hexagonal wurtzite) of different shapes under various conditions: fabrication and characterization, *Mater. Res. Express*, 2019, **6**, 085057.
54 E. Przeździecka, A. Lysak, A. Adhikari, M. Stachowicz, A. Wierzbicka, R. Jakiela, Z. Khosravizadeh, P. Sybilski and A. Kozanecki, Influence of the growth temperature and annealing on the optical properties of $\{CdO/ZnO\}_{30}$ superlattices, *J. Lumin.*, 2024, **269**, 120481.
55 C. S. Lee, K. A. Matori, S. H. A. Aziz, H. M. Kamari, I. Ismail and M. H. M. Zaid, Influence of zinc oxide on the physical,

structural and optical band gap of zinc silicate glass system from waste rice husk ash, *Optik*, 2017, **136**, 129–135.

56 T. N. Tran, T. V. A. Pham, M. L. P. Le, T. P. T. Nguyen and V. M. Tran, Synthesis of amorphous silica and sulfonic acid functionalized silica used as reinforced phase for polymer electrolyte membrane, *Adv. Nat. Sci.:Nanosci. Nanotechnol.*, 2013, **4**, 045007.

57 S. Luo, L. Xiong, H. Wang, Y. Li and H. Lu, Designing color controllable SiO2 amorphous colloidal arrays, *Ceram. Int.*, 2024, **50**(3), 5562–5569.

58 A. E. Noua, D. Kaya, G. Sigircik, T. Tuken, F. Karadag and A. Ekicibil, Enhanced photocatalytic activity in AgCu-decorated ZnO nanoparticles under UV and sunlight, *J. Mater. Sci.: Mater. Electron.*, 2024, **35**, 1220.

59 K. R. S. Murthy, G. K. Raghu and P. Binnal, Zinc Oxide Nanostructured Material for Sensor Application, *J. Adv. Biotechnol. Bioeng.*, 2021, **5**(1), 25–29.

60 S. Bashir, M. S. Awan, M. A. Farrukh, R. Naidu, S. A. Khan, N. Rafique, S. Ali, I. Hayat, I. Hussain and M. Z. Khan, In-vivo (Albino Mice) and in-vitro Assimilation and Toxicity of Zinc Oxide Nanoparticles in Food Materials, *Int. J. Nanomed.*, 2022, **17**, 4073–4085.

61 J. Li, J. Guo and H. Dai, Probing dissolved CO_2(aq) in aqueous solutions for CO_2 electro-reduction and storage, *Sci. Adv.*, 2022, **8**(19), eabo0399.

62 L. Qi, M. Babucci, Y. Zhang, A. Lund, L. Liu, J. Li, Y. Chen, A. S. Hoffman, S. R. Bare, Y. Han, B. C. Gates and A. T. Bell, Propane Dehydrogenation Catalyzed by Isolated Pt Atoms in ≡SiOZn–OH Nests in Dealuminated Zeolite Beta, *J. Am. Chem. Soc.*, 2021, **143**(50), 21364–21378.

63 N. A. Galedari, M. Rahmani and M. Tasbihi, Preparation, characterization, and application of ZnO@SiO_2 core–shell structured catalyst for photocatalytic degradation of phenol, *Environ. Sci. Pollut. Res.*, 2017, **24**, 12655–12663.

64 H. A. Ezzat, M. A. Hegazy, R. Ghoneim, H. Y. Zahran, I. S. Yahia, H. Elhaes, A. Refaat and M. A. Ibrahim, DFT and QSAR studies of PTFE/ZnO/SiO2 nanocomposite, *Sci. Rep.*, 2023, **11**, 9696.

65 Y. Zhang, X. Liu, M. Yusoff and M. H. Razali, Photocatalytic and Antibacterial Properties of a 3D Flower-Like TiO_2 Nanostructure Photocatalyst, *Scanning*, 2021, 3839235.

66 X. Fang, V. Viteri-Pflucker, A. H. King, J. Wang, J. Yan, L. Ke and L. Zhou, Oscillating Grain Boundaries and Their Effects on Grain Growth: Observations in Skyrmion Bicrystals, *Acta Mater.*, 2025, **290**, 120965.